NANO LETTERS

Letter

pubs.acs.org/NanoLett

Imaging the Localized Plasmon Resonance Modes in Graphene Nanoribbons

F. Hu,[†,#] Y. Luan,[†,#] Z. Fei,[*,†] I. Z. Palubski,[†] M. D. Goldflam,[‡,§] S. Dai,[‡] J.-S. Wu,[‡] K. W. Post,[‡] G. C. A. M. Janssen,[∥] M. M. Fogler,[‡] and D. N. Basov[‡,⊥]

[†]Department of Physics and Astronomy, U.S. DOE Ames Laboratory, Iowa State University, Ames, Iowa 50011, United States

[‡]Department of Physics, University of California at San Diego, La Jolla, California 92093, United States

[§]Sandia National Laboratories, Albuquerque, New Mexico 87185, United States

[∥]Department of Precision and Microsystems Engineering, Delft University of Technology, Mekelweg 2, 2628 CD Delft, Netherland

[⊥]Department of Physics, Columbia University, New York, New York 10027, United States

Supporting Information

ABSTRACT: We report a nanoinfrared (IR) imaging study of the localized plasmon resonance modes of graphene nanoribbons (GNRs) using a scattering-type scanning near-field optical microscope (s-SNOM). By comparing the imaging data of GNRs that are aligned parallel and perpendicular to the in-plane component of the excitation laser field, we observed symmetric and asymmetric plasmonic interference fringes, respectively. Theoretical analysis indicates that the asymmetric fringes are formed due to the interplay between the localized surface plasmon resonance (SPR) mode excited by the GNRs and the propagative surface plasmon polariton (SPP) mode launched by the s-SNOM tip. With rigorous simulations, we reproduce the observed fringe patterns and address quantitatively the role of the s-SNOM tip on both the SPR and SPP modes. Furthermore, we have seen real-space signatures of both the dipole and higher-order SPR modes by varying the ribbon width.

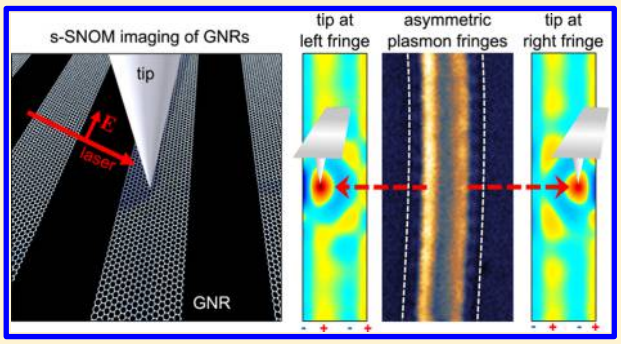

KEYWORDS: *s-SNOM, graphene nanoribbons, surface plasmon polariton, surface plasmon resonance, asymmetric fringes*

Graphene plasmon polaritons are collective oscillations of Dirac Fermions in graphene with photons, which possess many superior characteristics such as high confinement, electrical tunability, long lifetime, and a strong promise for nanophotonic applications in the terahertz to infrared (IR) regime.[1−8] Because of their finite momentum, plasmons in large-area homogeneous graphene films cannot be excited directly by far-field photons. In order to bridge the momentum gap between photons and plasmons, one could take advantage of the scattering-type scanning near-field optical microscope (s-SNOM)[9−18] or pattern graphene into various forms of plasmonic nanostructures,[19−30] for example, graphene nanoribbons (GNRs) in the current work. In the former case, the s-SNOM is capable of launching and mapping the interference fringes of propagative surface plasmon polaritons (SPPs) in graphene. In the latter case, graphene nanostructures can excite the localized surface plasmon resonance (SPR) modes when illuminated directly by the IR beam. Recently, nano-IR imaging studies of various types of graphene nanostructures were reported, which addressed mainly the tip-launched surface and edge plasmons.[31−34] On the other hand, real-space imaging studies of the SPR modes have not been reported so far.

Here, by combining the s-SNOM technique with rigorous numerical modeling, we performed a nano-IR imaging study of the localized SPR modes in GNRs. The samples that we investigated are GNR arrays (Figure 1a,e) fabricated by lithographic patterning of chemical-vapor-deposited (CVD) graphene single crystals[35,36] on Al_2O_3 substrates (Supporting Information). Our s-SNOM apparatus, built on a tapping-mode atomic force microscope (AFM), is capable of simultaneously collecting nano-IR and AFM images of the samples. In our experiments, we utilized a metalized AFM tip with a radius of curvature of ∼25 nm at the tip apex. As will be discussed below, such a sharp tip acts as a plasmon launcher, enhancer, and scatter. For IR excitation, we use a p-polarized mid-IR beam from a continuous-wave (CW) laser. The excitation laser frequency is set to be at ω = 1184 cm^{-1}, corresponding to a photon energy of about 147 meV. The experimental observables are the near-field amplitude (s) and phase (ψ) demodulated at the third harmonics of the tapping frequency of the tip in order to suppress the background signal. In the current work, we discuss mainly the s signal that scales monotonically with the plasmon field amplitude underneath the

Received: May 15, 2017
Revised: August 7, 2017
Published: August 14, 2017

DOI: 10.1021/acs.nanolett.7b02029
Nano Lett. 2017, 17, 5423−5428

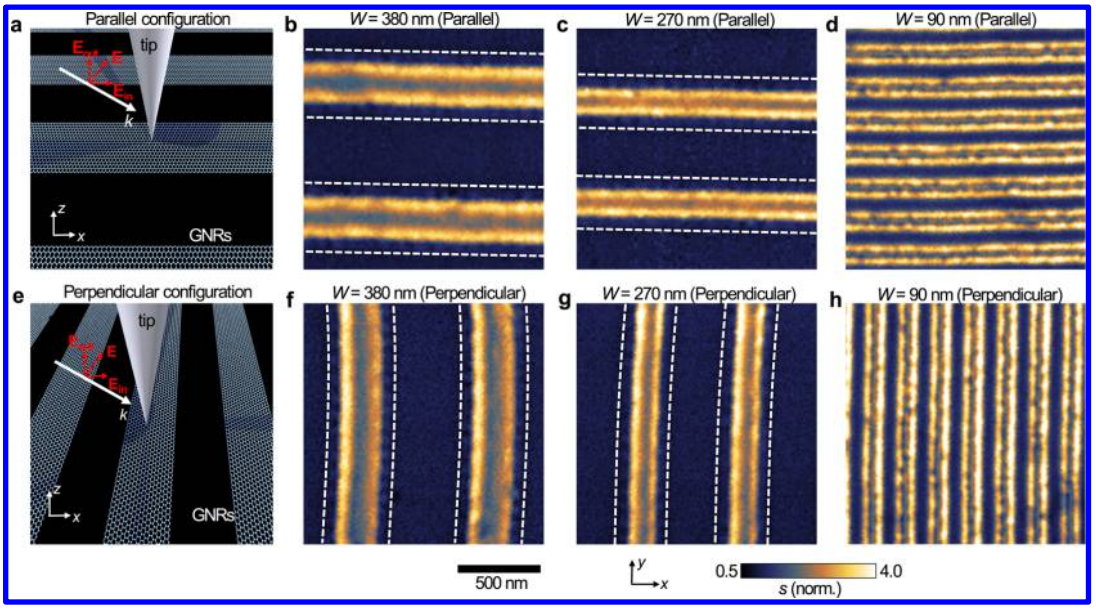

Figure 1. Nano-IR imaging of GNRs in two laser excitation configurations. (a) Schematics of the nano-IR imaging experiment of GNRs in the parallel configuration. (b–d) Nano-IR imaging data of GNRs with widths of 380, 270, and 90 nm, respectively, taken in the parallel configuration. (e) Schematics of the nano-IR imaging experiment of GNRs in the perpendicular configuration. (f–h) Nano-IR imaging data of GNRs with widths of 380, 270, and 90 nm, respectively, taken in the perpendicular configuration. The excitation laser frequency is set to be ω = 1184 cm^{-1}. The dashed lines in panels b,c,f,g mark the edges of the ribbons. In panels d,h, the ribbon edges coincide with the bright fringes.

AFM tip.[9−18] All our experiments were conducted at ambient conditions.

To explore the plasmonic responses due to the localized SPR modes in GNRs, we consider two excitation configurations in our experiments for a case-control comparison. In the first configuration (Figure 1a), the p-polarized laser beam is aligned along the edges of the ribbons, and thus the in-plane (x–y plane) component of the laser field ($\mathbf{E}_{in}$) is parallel to the ribbons (referred to as "parallel configuration" below). In this configuration, the SPR modes solely due to the ribbons are not excited and therefore we are probing primarily tip-launched SPP modes. In the second configuration (Figure 1e), the GNRs are rotated in-plane by 90°, so $\mathbf{E}_{in}$ is perpendicular to the ribbons (referred to as "perpendicular configuration" below). In this latter configuration, both the SPR and SPP modes can be excited. The nano-IR imaging data of GNRs with three different widths (W = 380, 270, and 90 nm) taken at both configurations are shown in Figure 1b–d and Figure 1f–h, where we plot the near-field amplitude s normalized to that of the Al_2O_3 substrate.

The dominant features in the nano-IR images (Figure 1) are the bright fringes aligned parallel to the ribbon edges. We first discuss the parallel configuration (Figure 1b–d), where the bright fringes are solely due to the tip-launched SPP modes.[31] For all the images in Figure 1b–d, we found two bright fringes with roughly equal intensity for each ribbon, but the locations of the fringes show sensitive dependence on the ribbon width (see also the calculated fringe profiles in Figure S2). For relatively wide ribbons (W = 380 and 270 nm), the bright fringes are located fully inside the ribbons. In contrast, for the narrowest ribbons (W = 90 nm), the peak fringe signal is right at the ribbon edges with plasmon field extending beyond graphene. Figure 2 displays the line cuts (solid curves) across the fringes extracted from the nano-IR images in Figure 1. The peaks in the profiles correspond to the fringes in the nano-IR images and the vertical dashed lines mark the edges of the ribbons. According to the earlier studies,[9−18] the bright fringes

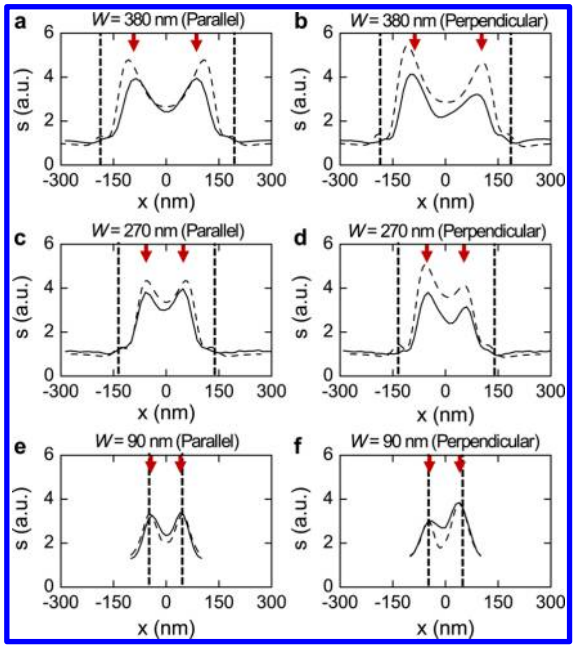

Figure 2. Line profiles across the plasmonic fringes in GNRs from both experiment (solid curves) and theory (dashed curves) taken on (a) 380 nm wide GNRs in the parallel configuration, (b) 380 nm wide GNRs in the perpendicular configuration, (c) 270 nm wide GNRs in the parallel configuration, (d) 270 nm wide GNRs in the perpendicular configuration, (e) 90 nm wide GNRs in the parallel configuration, and (f) 90 nm wide GNRs in the perpendicular configuration. The vertical dashed lines mark the edges of GNRs and the arrows mark the locations of the peaks due to the fringes. The plotted near-field amplitude signal is normalized to that of the Al_2O_3 substrate.

are formed due to the constructive interference between tip-launched SPPs and those reflected back from the edges. Note that there is a constant plasmon phase shift ($\phi \approx -0.8\pi$) upon reflection off the graphene edges.[37,38] As a result, the first bright

DOI: 10.1021/acs.nanolett.7b02029
Nano Lett. 2017, 17, 5423−5428

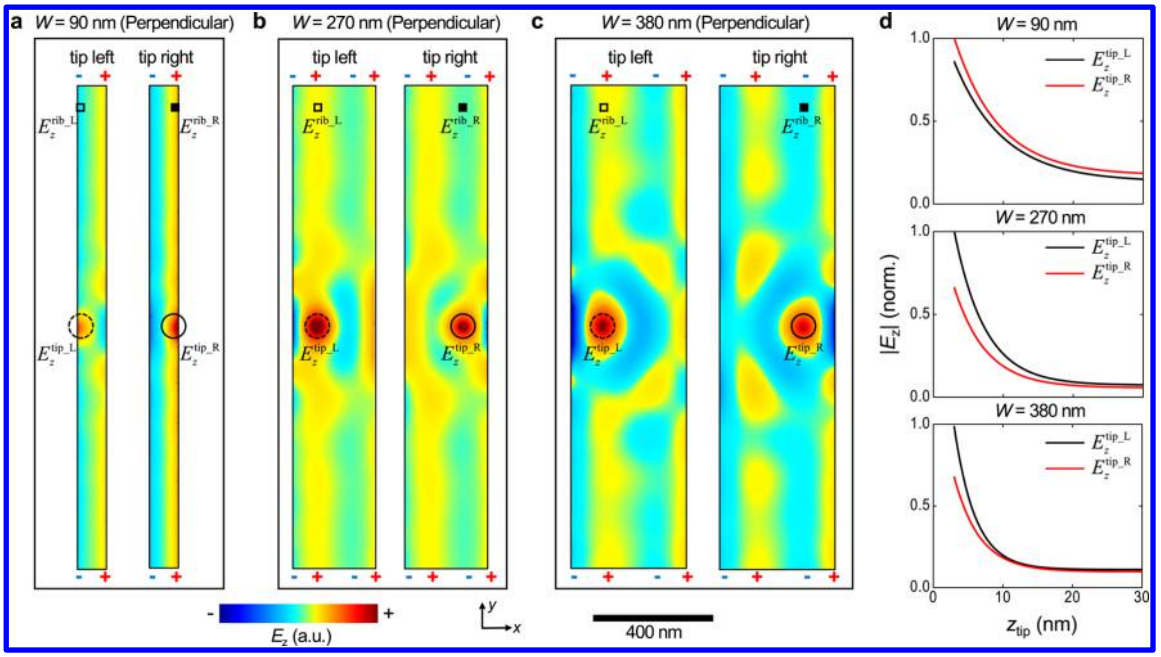

Figure 3. Comsol simulation of the plasmon field maps the GNRs in the perpendicular configuration. (a–c) Modeled plasmon field maps of GNRs with various widths, where we plot the snapshots of z-direction electric field (E_z) right above the graphene surface at z = 0. The left and right panels in a–c are simulations with tips at the locations of the left and right fringes (see Figure 1f–h and Figure 2b,d,f), respectively. The circles mark the locations of tip: ±42 nm, ±55 nm, and ±88 nm for W = 90 nm, 270, and 380 nm, respectively. The tip–sample separation (z_{tip}) is set to be 15 nm. $E_z^{tip\_L}$ and $E_z^{tip\_R}$ correspond to the E_z field at the center of the dashed and solid circles, respectively. $E_z^{rib\_L}$ and $E_z^{rib\_R}$ correspond to the E_z field at locations of the hollow and solid squares, respectively. (d) Simulated z_{tip}-dependence curves of the $|E_z^{tip\_L}|$ (black curves) and $|E_z^{tip\_R}|$ (red curves) for GNRs with various widths. Here, the field amplitude is normalized to the maximum value of each panel.

fringe (or the principal fringe as termed in ref 31) due to each edge is about $0.4\lambda_p$ away from the edge, where λ_p is the plasmon wavelength. The subsequent fringes are not clearly seen here due to the limited width of our ribbons. In our typical samples, the separation between the principal fringe and the edge ($\sim 0.4\lambda_p$) is roughly 100 nm. Therefore, for wide ribbons (W = 380 or 270 nm) the two principal fringes due to both edges are located inside the ribbons. In contrast, for the 90 nm wide ribbons, the principal fringes appear close to the opposite edge. For instance, the fringe formed due to plasmon reflection off the left edge will appear on the right side of the ribbon and vice versa (Figures 1d and 2e).

In the case of perpendicular configuration (Figure 1f–h), at first glance the general patterns of the fringes are similar to those in the parallel configuration. Closer inspection reveals an important difference: the intensities of the two fringes for each ribbon are not identical. This can be seen more clearly in the fringes profiles (solid curves) plotted in Figure 2. In contrast to the symmetric profiles in the parallel configuration (Figure 2a,c,e), the fringe profiles in the perpendicular configuration show clear asymmetry (Figure 2b,d,f). Moreover, the ribbons with different widths are not asymmetric in the same way. For ribbons with widths of W = 380 and 270 nm, the left fringe is stronger, whereas for the 90 nm wide ribbon, the right fringe is stronger. We wish to emphasize that the observed asymmetric plasmon fringes in the imaging data are the real-space signatures of the ribbon-excited SPR modes, and the type of fringe asymmetry (left fringe stronger or right fringe stronger) is associated with SPR modes with different orders. We will demonstrate that with detailed modeling and analysis in the remaining part of the paper.

Our modeling and analysis are based on two types of simulations. The first type of simulation is for quantitative calculations of the s-SNOM signal using a model coded in Matlab. In this model, the tip is approximated as an elongated metallic spheroid (Figure S1) and we evaluate numerically the total radiating dipole ($\mathbf{p}$) of the coupled tip–sample system. The optical conductivity of graphene was obtained with the random phase approximation method where Fermi energy of graphene E_F is set to be 0.37 eV to match our data. To calculate the third harmonic near-field signals, we considered tip modulation and demodulation processes by computing $\mathbf{p}$ at multiple tip–sample separations (z_{tip}). The real-space profiles of the near-field amplitude were obtained by varying the x-locations of the tip in the calculations. The calculated fringe profiles are plotted in Figure 2 as dashed curves, which are consistent with the experimental profiles (solid). Additional simulation results are presented in Figure S2, where one can see that more fringes appear as ribbon width increases and the fringe asymmetry is a common characteristic for GNRs with all widths under perpendicular configuration. We emphasize that considering both the SPR and SPP modes when calculating $\mathbf{p}$ is critical for modeling the asymmetric profiles (Supporting Information).

To visualize in real space the two types of plasmonic modes and how they couple together to form the asymmetric fringes, we performed the second type of simulation using a frequency-domain finite-element model based on Comsol Multiphysics.[32,38] In this simulation, the tip is again approximated as a conducting spheroid and graphene is treated as an effective thin metal layer (Supporting Information). Figure 3 presents the Comsol-simulated spatial maps of GNRs underneath the s-SNOM tip (located at the center of the circles), where we plot the snapshots of the z-component electric field (E_z) on the sample surface in the perpendicular configuration. At the snapshot time (t_0), the out-of-plane component of the far-field

DOI: 10.1021/acs.nanolett.7b02029
Nano Lett. 2017, 17, 5423–5428

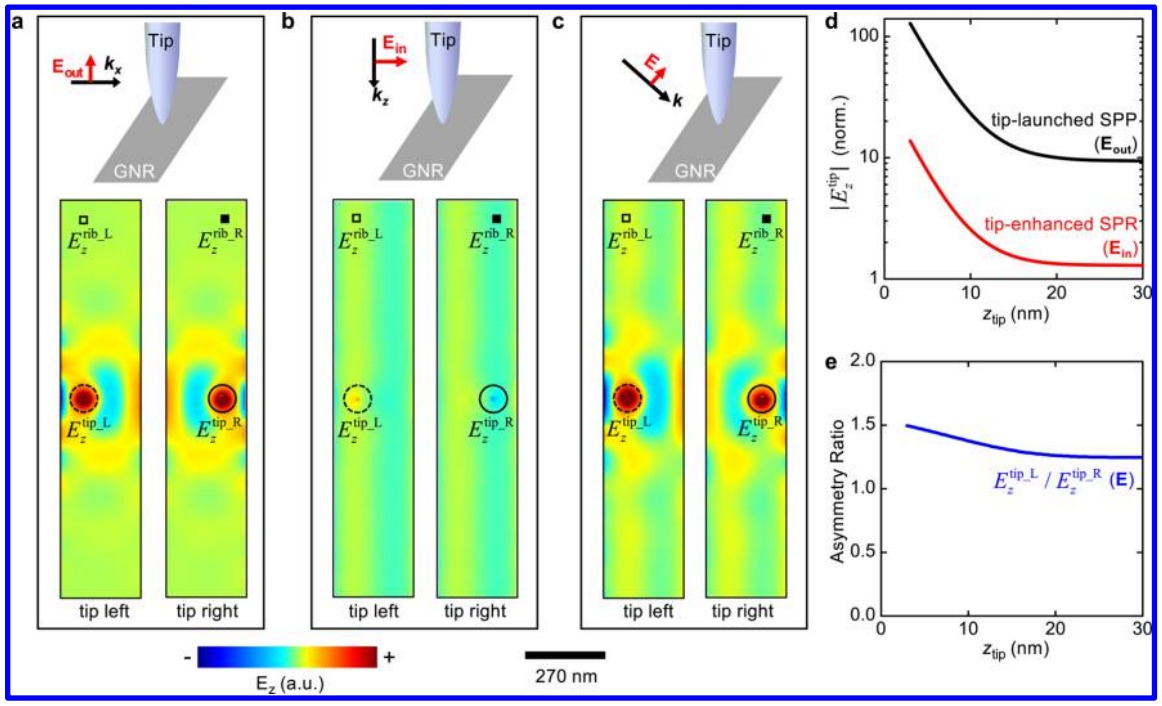

Figure 4. Simulated plasmon field maps of the 270 nm wide ribbon revealing tip-enhancement effect. (a) Simulated plasmon field map of the 270 nm wide ribbon considering solely the out-of-plane incident field. (b) Simulated plasmon field map considering solely the in-plane incident field. (c) Simulated plasmon field map considering full incident field. The left and right panels in a–c are simulations with tips at the locations of the left and right fringes (see Figure 1f–h and Figure 2b,d,f), respectively. The tip–sample separation (z_{tip}) is set to be 5 nm. (d) Simulated z_{tip}-dependence curves of $|E_z^{tip}|$ due to the tip-launched SPP mode (black, under $\mathbf{E}_{out}$ excitation) and the tip-enhanced SPR mode (red, under $\mathbf{E}_{out}$ excitation). (e) Simulated z_{tip}-dependence curve of the asymmetry ratio: $E_z^{tip\_L}/E_z^{tip\_R}$ under full-field ($\mathbf{E}$) excitation.

excitation field ($\mathbf{E}_{out}$) (Figure 1a,e) is pointing upward toward the positive z direction, so the E_z field right underneath the tip is positive. There are two reasons that we focus on the E_z field. First, E_z field right above the sample surface is proportional to surface charge density, thus suitable for describing collective oscillations of charges, namely plasmons. Second, the E_z field underneath the tip (marked with circles in Figure 3) is roughly proportional to the near-field signal collected by the s-SNOM at this particular sample location. For comparison, we performed two sets of simulations on each GNR, where the x-coordinates of the modeled tip (x_{tip}) are set to be equal to those of the left and right fringe peaks in Figure 2 ($x_{tip} = \pm 42$, ± 55, and ± 88 nm for $W = 90$, 270, and 380 nm respectively). The tip–sample separation z_{tip} is set to be 15 nm in Figure 3a–c. Such a z_{tip} setting enables clear visualization of both the SPR mode and SPP mode within the same field map (smaller z_{tip} leads to much stronger SPP mode that outshines by orders of magnitude the pure SPR mode). The key message related to fringe asymmetry are qualitatively similar at other z_{tip} settings (see Figure 3d and discussions below).

We first pay attention to the sample regions far away from the tip (e.g., top and bottom ends of GNRs in Figure 3a–c), where the tip-launched SPP modes are completely damped due to the limited plasmon propagation length ($L_p \ll 1\ \mu$m) of our samples, so the pure SPR modes dominate here. Indeed, the field patterns here are similar to those of simulations considering solely GNRs (Figure S5). For the 90 nm wide ribbon, the E_z field changes from negative (−) on the left side to positive (+) on the right side. For both the 270 and 380 nm wide ribbons, the E_z field appears to be −, + , − and + from left to right. According to previous studies, the above field patterns correspond to SPR modes with order indexes $n = 0$ and $n = 2$ in the resonance condition equation: $2q_pW + 2\phi = 2\pi n$, where q_p is the plasmon wavevector and $\phi \approx -0.8\pi$ is plasmon phase shift upon reflection at the sample edge.[37,38] In Figure S4, we plot a simulated W-dependent far-field absorption curve with Comsol, where the first two resonance peaks correspond to $n = 0$ and 2. These resonance peaks (Figure S4) have significant broadening due to the plasmon damping, so both the 270 and 380 nm wide ribbons excite the $n = 2$ SPR mode (Figure S4). Note that the E_z field of these even-integer ($n = 0$, 2...) modes at the left fringe location ($E_z^{rib\_L}$, marked with hollow square) is opposite compared to that at the right fringe location ($E_z^{rib\_R}$, marked with solid square). As discussed later in the paper, the opposite signs of $E_z^{rib\_L}$ and $E_z^{rib\_R}$ is critical for the formation of asymmetric fringes. In fact, there are also odd-integer SPR modes ($n = 1$, 3...) existing, but they cannot be excited directly by the far-field optical beam in the perpendicular configuration. They could possibly be launched by the s-SNOM tip as waveguide modes[1,39–41] propagating along the direction of the ribbons (see discussions below).

The field patterns become more complicated closer to location of the tip (marked with circles in Figure 3), where tip-launched SPP modes dominate. The SPP modes propagate in all directions away from the tip. Those that propagate in the transverse direction of the ribbons (namely x-direction) will reach the ribbon edge, reflect back, and generate interference fringes that are imaged by the s-SNOM (Figures 1 and 2). The plasmon modes could also propagate along the direction of the ribbons (namely y direction) as waveguide modes[1,39–41] or edge modes,[31,32] which are responsible for the complicated field patterns extending several hundred nanometers away from the tip in Figure 3. Note that the waveguide modes simply propagate away from the tip and do not reveal themselves as

DOI: 10.1021/acs.nanolett.7b02029
Nano Lett. 2017, 17, 5423–5428

interference fringes in the s-SNOM images. On the other hand, the edge plasmons do generate edge signal oscillations in the s-SNOM images due to the scattering by the edge defects that exist commonly at lithography-patterned graphene edges.[31,32] Nevertheless, they are extremely weak and can only been seen with adjusted color scales (Figure S7a). Therefore, edge plasmons only have minor effects on the fringe patterns and profiles (Figure S7b).

We now discuss the E_z field right underneath the tip (E_z^{tip}) that is directly linked to the near-field amplitude signal collected by the s-SNOM. More specifically, we compare in Figure 3 the E_z^{tip} values at the left fringe location ($E_z^{tip\_L}$, at the center of the dashed circle) with that at the right fringe location ($E_z^{tip\_R}$, at the center of the solid circle). First, we notice that both $E_z^{tip\_L}$ and $E_z^{tip\_R}$ are positive for all the field maps in Figure 3. On the other hand, $E_z^{tip\_L}$ is clearly different from $E_z^{tip\_R}$. For the 90 nm wide ribbon (Figure 3a), $E_z^{tip\_L}$ is weaker than $E_z^{tip\_R}$. For the 270 and 380 nm wide ribbons (Figure 3b,c) on the other hand, $E_z^{tip\_L}$ is stronger than $E_z^{tip\_R}$. Such an inequality between $E_z^{tip\_L}$ and $E_z^{tip\_R}$ remains the same in simulations with other values of z_{tip} (Figure 3d). Therefore, the near-field amplitude (s) at the two fringe locations are expected to share the same inequality, which were observed in our s-SNOM experiments (Figures 1 and 2). We have also performed Comsol simulations in the parallel excitation configuration (Figure S6), where no ribbon-excited SPR modes are present. Here we found that $E_z^{tip\_L}$ is equal to $E_z^{tip\_R}$ for all the GNRs, which is in agreement with the symmetric fringe patterns observed in Figure 1b–d.

So far, the SPR mode coexists with the SPP mode in the field maps in Figure 3. In order to decouple them to explore their specific roles on the fringe patterns, we performed a new set of field simulations with solely the out-of-plane component ($\mathbf{E}_{out}$, Figure 4a), the in-plane component ($\mathbf{E}_{in}$, Figure 4b) of the excitation field as well as the total excitation field ($\mathbf{E} = \mathbf{E}_{out} + \mathbf{E}_{in}$, Figure 4c). Here in Figure 4, we take the 270 nm-wide ribbon as an example (ribbons with other widths are discussed in the following paragraphs). The tip–sample separation is set to be z_{tip} = 5 nm to highlight the role of the tip on plasmons inside the ribbons. Results with other z_{tip} settings are discussed in Figure 4d,e. For the purpose of quantitative analysis, we plot in Table 1 the numbers of $E_z^{rib\_L}$, $E_z^{rib\_R}$, $E_z^{tip\_L}$, and $E_z^{tip\_R}$ extracted directly from Figure 4a–c. Note that all the E_z numbers in Table 1 are corrected from the far-field background (namely $|\mathbf{E}_{out}|$), and they are normalized to the field amplitude of the pure SPR mode of the 270 nm-wide GNR: $|E_z^{rib\_L}| = |E_z^{rib\_R}| = 1$ in Figure 4b.

Table 1. Extracted E_z Field Values at Various Marked Locations in Figure 4a–c

GNR (270 nm)	$E_z^{rib\_L}$	$E_z^{rib\_R}$	$E_z^{tip\_L}$	$E_z^{tip\_R}$
$\mathbf{E}_{out}$ excitation	0	0	63	63
$\mathbf{E}_{in}$ excitation	1	−1	7	−7
$\mathbf{E}$ excitation	1	−1	71	53

With solely $\mathbf{E}_{out}$ excitation (Figure 4a), the SPR modes are not excited, so we can examine the pure SPP mode. Here we find that the E_z^{tip} field values at the two fringe locations are equal to each other: $E_z^{tip\_L} = E_z^{tip\_R} \approx 63$. With solely $\mathbf{E}_{in}$ excitation (Figure 4b), the SPP modes are not launched, so we can study the pure SPR mode and their response to the tip. Indeed, from Figure 4b we find that the SPR mode (n = 2) is excited in the ribbons. Away from the tip, the pure SPR field at the two fringe locations (marked with squares) is opposite to each other: $E_z^{rib\_L} = 1$ and $E_z^{rib\_R} = -1$. At the tip location, the SPR field is enhanced by the tip: $E_z^{tip\_L} \approx 7$ and $E_z^{tip\_R} = -7$. By superposing E_z^{tip} under both $\mathbf{E}_{in}$ and $\mathbf{E}_{out}$ excitations, we have $E_z^{tip\_L} \approx 63 + 7 = 70$ and $E_z^{tip\_R} \approx 63-7 = 56$, yielding an asymmetric ratio of $E_z^{tip\_L}/E_z^{tip\_R} \approx 70/56 \approx 1.25$. This is in agreement with the simulation with direct full-field ($\mathbf{E}$) excitation (Figure 4c), where the asymmetric ratio is $E_z^{tip\_L}/E_z^{tip\_R} = 71/53 \approx 1.34$. The slight deviation (~7%) between the two ratios is likely due the numerical error of Comsol simulation (Supporting Information). The field amplitude values of both the tip-launched SPP mode ($\mathbf{E}_{out}$ excitation) and the tip-enhanced SPR mode ($\mathbf{E}_{in}$ excitation) increases exponentially with decreasing z_{tip} (Figure 4d) but the asymmetry ratio ($E_z^{tip\_L}/E_z^{tip\_R}$) under full-field ($\mathbf{E}$) excitations varies gently from 1.25 to 1.5 (Figure 4e). Such an asymmetric ratio agrees with our experimental fringe profile (Figure 2b) where the left peak is about 30–35% higher than the right peak.

On the basis of the above discussions, we can conclude that the superposition of the tip-launched SPP mode and the tip-enhanced SPR mode is the origin of the formation of the asymmetric fringes. There are three key ingredients in this statement. First, the SPR modes (n = 0 and 2) have opposite E_z fields at the two fringe locations (Figure 3 and Figure S5). For the 270 and 380 nm wide GNRs that supports the n = 2 SPR mode, $E_z^{rib\_L} > 0$ and $E_z^{rib\_R} < 0$. Whereas for the 90 nm wide GNRs that supports the n = 0 SPR mode $E_z^{rib\_L} < 0$ and $E_z^{rib\_R} > 0$. Note that the SPP field underneath the tip is always positive. Second, tips strongly enhance the SPR mode. Without the strong enhancement by a metallic s-SNOM tip, the pure SPR mode with a field amplitude of $|E_z| = 1$ is orders of magnitude weaker than the SPP mode underneath the tip (Figure 4d) and is thus too weak to be detected. Third, the strong SPP mode acts as an interferometric amplifier for the SPR signal. It could further amplify the signal by adding (when $E_z^{rib} > 0$) or subtracting (when $E_z^{rib} < 0$) tip-enhanced SPR mode. The outcome is the stronger right fringe in the 90 nm wide ribbon (n = 0 SPR mode) and the stronger left fringe in the two wider ribbons (n = 2 SPR mode), which were observed by our nano-IR imaging experiment.

By combining the state-of-the-art s-SNOM technique with rigorous simulations, we performed a nano-IR imaging study of the localized SPR modes in GNRs. These resonance modes, strongly enhanced by the s-SNOM tip, couple with the tip-launched SPPs to form asymmetric plasmonic fringes under perpendicular excitation configurations. Moreover, by varying the GNR widths, we saw evidence of both the dipole and higher-order SPR modes. The distinct field patterns of these modes lead to an opposite fringe asymmetry. Our study provides a new scheme for studying the SPR modes in GNRs and sheds light on future studies of resonance behaviors in other novel nanophotonic media beyond graphene.

■ ASSOCIATED CONTENT

Supporting Information

The Supporting Information is available free of charge on the ACS Publications website at DOI: 10.1021/acs.nanolett.7b02029.

Detailed information about experiments and simulations (PDF)

DOI: 10.1021/acs.nanolett.7b02029
Nano Lett. 2017, 17, 5423–5428

AUTHOR INFORMATION

Corresponding Author

*E-mail: (Z.F) zfei@iastate.edu.

ORCID

Z. Fei: 0000-0002-7940-5566

S. Dai: 0000-0001-7259-7182

Author Contributions

#F.H. and Y.L. contributed equally to this work.

Notes

The authors declare no competing financial interest.

ACKNOWLEDGMENTS

Authors acknowledge support from ONR and AFOSR. The development of scanning plasmon interferometry is supported by DOE-BES and ARO. F.H., Y.L., and Z.F. are supported by Iowa State University and W. M. Keck foundation. Work at the Ames Laboratory was supported by the Department of Energy-Basic Energy Sciences under Contract No. DE-AC02-07CH11358. D.N.B. is supported by the Gordon and Betty Moore Foundation's EPiQS Initiative through Grant GBMF4533. G.C.A.M.J. acknowledges Foundation for Fundamental Research on Matter (FOM) and Netherlands Organisation for Scientific Research (NWO).

REFERENCES

(1) Vakil, A.; Engheta, N. *Science* **2011**, *332*, 1291−1294.

(2) Jablan, M.; Buljan, H.; Soljačić, M. *Phys. Rev. B: Condens. Matter Mater. Phys.* **2009**, *80*, 245435.

(3) Koppens, F. H. L.; Chang, D. E.; García de Abajo, F. J. *Nano Lett.* **2011**, *11*, 3370−3377.

(4) Grigorenko, A. N.; Polini, M.; Novoselov, K. S. *Nat. Photonics* **2012**, *6*, 749.

(5) Basov, D. N.; Fogler, M. M.; Lanzara, A.; Wang, F.; Zhang, Y. *Rev. Mod. Phys.* **2014**, *86*, 959.

(6) Basov, D. N.; Fogler, M. M.; García de Abajo, F. J. *Science* **2016**, *354*, aag1992.

(7) Low, T.; Avouris, P. *ACS Nano* **2014**, *8*, 1086.

(8) Low, T.; Chaves, A.; Caldwell, J. D.; Kumar, A.; Fang, N. X.; Avouris, P.; Heinz, T. F.; Guinea, F.; Martin-Moreno, L.; Koppens, F. H. L. *Nat. Mater.* **2016**, *16*, 182−194.

(9) Fei, Z.; Andreev, G. O.; Bao, W.; Zhang, L. M.; McLeod, A. S.; Wang, C.; Stewart, M. K.; Zhao, Z.; Dominguez, G.; Thiemens, M.; Fogler, M. M.; Tauber, M. J.; Castro-Neto, A. H.; Lau, C. N.; Keilmann, F.; Basov, D. N. *Nano Lett.* **2011**, *11*, 4701−4705.

(10) Fei, Z.; Rodin, A. S.; Andreev, G. O.; Bao, W.; McLeod, A. S.; Wagner, M.; Zhang, L. M.; Zhao, Z.; Thiemens, M.; Dominguez, G.; Fogler, M. M.; Castro Neto, A. H.; Lau, C. N.; Keilmann, F.; Basov, D. N. *Nature* **2012**, *487*, 82−85.

(11) Chen, J.; Badioli, M.; Alonso-Gonzalez, P.; Thongrattanasiri, S.; Huth, F.; Osmond, J.; Spasenovic, M.; Centeno, A.; Pesquera, A.; Godignon, P.; Elorza, A. Z.; Camara, N.; García de Abajo, F. J.; et al. *Nature* **2012**, *487*, 77−81.

(12) Fei, Z.; Rodin, A. S.; Gannett, W.; Dai, S.; Regan, W.; Wagner, M.; Liu, M. K.; McLeod, A. S.; Dominguez, G.; Thiemens, M.; Castro Neto, A. H.; Keilmann, F.; Zettl, A.; Hillenbrand, R.; Fogler, M. M.; Basov, D. N. *Nat. Nanotechnol.* **2013**, *8*, 821−825.

(13) Alonso-Gonzalez, P.; Nikitin, A. Y.; Golmar, F.; Centeno, A.; Pesquera, A.; Velez, S.; Chen, J.; Navickaite, G.; Koppens, F.; Zurutuza, A.; Casanova, F.; Hueso, L. E.; Hillenbrand, R. *Science* **2014**, *344*, 1369−1373.

(14) Woessner, G.; Lundeberg, M. B.; Gao, Y.; Principi, A.; AlonsoGonzalez, P.; Carrega, M.; Watanabe, K.; Taniguchi, T.; Vignale, G.; Polini, M.; Hone, J.; Hillenbrand, R.; Koppens, F. H. L. *Nat. Mater.* **2014**, *14*, 421−425.

(15) Gerber, J. A.; Berweger, S.; O'Callahan, B. T.; Raschke, M. B. *Phys. Rev. Lett.* **2014**, *113*, 055502.

(16) Wagner, M.; Fei, Z.; McLeod, A. S.; Rodin, A. S.; Bao, W.; Iwinski, E. G.; Zhao, Z.; Goldflam, M.; Liu, M. K.; Dominguez, G.; Thiemens, M.; Fogler, M. M.; Castro Neto, A. H.; Lau, C. N.; Amarie, S.; Keilmann, F.; Basov, D. N. *Nano Lett.* **2014**, *14*, 894−900.

(17) Ni, G. X.; Wang, L.; Goldflam, M. D.; Wagner, M.; Fei, Z.; McLeod, A. S.; Liu, M. K.; Keilmann, F.; Özyilmaz, B.; Castro Neto, A. H.; Hone, J.; Fogler, M. M.; Basov, D. N. *Nat. Photonics* **2016**, *10*, 244−247.

(18) Alonso-González, P.; Nikitin, A. Y.; Gao, Y.; Woessner, A.; Lundeberg, M. B.; Principi, A.; Forcellini, N.; Yan, W.; Vélez, S.; Huber, A. J.; Watanabe, K.; Taniguchi, T.; Casanova, F.; Hueso, L. E.; Polini, M.; Hone, J.; Koppens, F. H. L.; Hillenbrand, R. *Nat. Nanotechnol.* **2016**, *12*, 31−35.

(19) Popov, V. V.; Bagaeva, T. Y.; Otsuji, T.; Ryzhii, V. *Phys. Rev. B: Condens. Matter Mater. Phys.* **2010**, *81*, 073404.

(20) Ju, L.; Geng, B.; Horng, J.; Girit, C.; Martin, M.; Hao, Z.; Bechtel, H. A.; Liang, X.; Zettl, A.; Shen, Y. R.; Wang, F. *Nat. Nanotechnol.* **2011**, *6*, 630−634.

(21) Yan, H.; Li, X.; Chandra, B.; Tulevski, G.; Wu, Y.; Freitag, M.; Zhu, W.; Avouris, P.; Xia, F. *Nat. Nanotechnol.* **2012**, *7*, 330−334.

(22) Brar, V. W.; Jang, M. S.; Sherrott, M.; Lopez, J. J.; Atwater, H. A. *Nano Lett.* **2013**, *13*, 2541−2547.

(23) Fang, Z.; Thongrattanasiri, S.; Schlather, A.; Liu, Z.; Ma, L.; Wang, Y.; Ajayan, P.; Nordlander, P.; Halas, N. J.; Garcia de Abajo, F. J. *ACS Nano* **2013**, *7* (3), 2388−2395.

(24) Gao, W.; Shi, G.; Jin, Z.; Shu, J.; Zhang, Q.; Vajtai, R.; Ajayan, P. M.; Kono, J.; Xu, Q. *Nano Lett.* **2013**, *13*, 3698−3702.

(25) Yan, H.; Low, T.; Zhu, W.; Wu, Y.; Freitag, M.; Li, X.; Guinea, F.; Avouris, P.; Xia, F. *Nat. Photonics* **2013**, *7*, 394−399.

(26) Otsuji, T.; Popov, V.; Ryzhii, V. *J. Phys. D: Appl. Phys.* **2014**, *47*, 094006.

(27) Freitag, M.; Low, T.; Zhu, W.; Yan, H.; Xia, F.; Avouris, P. *Nat. Commun.* **2013**, *4*, 1951.

(28) Li, Y.; Yan, H.; Farmer, D. B.; Meng, X.; Zhu, W.; Osgood, R. M.; Heinz, T. F.; Avouris, P. *Nano Lett.* **2014**, *14* (3), 1573−1577.

(29) Rodrigo, D.; Limaj, O.; Janner, D.; Etezadi, D.; Garcia de Abajo, F. J.; Pruneri, V.; Altug, H. *Science* **2015**, *349*, 165−168.

(30) Hu, H.; Yang, X.; Zhai, F.; Hu, D.; Liu, R.; Liu, K.; Sun, Z.; Dai, Q. *Nat. Commun.* **2016**, *7*, 12334.

(31) Fei, Z.; Goldflam, M. D.; Wu, J.-S.; Dai, S.; Wagner, M.; McLeod, A. S.; Liu, M. K.; Post, K. W.; Zhu, S.; Janssen, G. C. A. M.; Fogler, M. M.; Basov, D. N. *Nano Lett.* **2015**, *15* (12), 8271−8276.

(32) Nikitin, A. Y.; Alonso-Gonzalez, P.; Velez, S.; Mastel, S.; Centeno, A.; Pesquera, A.; Zurutuza, A.; Casanova, F.; Hueso, L. E.; Koppens, F. H. L.; Hillenbrand, R. *Nat. Photonics* **2016**, *10*, 239−243.

(33) Fei, Z.; Foley, J. J., IV; Gannett, W.; Liu, M. K.; Dai, S.; Ni, G. X.; Zettl, A.; Fogler, M. M.; Wiederrecht, G. P.; Gray, S. K.; Basov, D. N. *Nano Lett.* **2016**, *16*, 7842−7848.

(34) Xu, Q.; Ma, T.; Danesh, M.; Shivananju, B. N.; Gan, S.; Song, J.; Qiu, C. W.; Cheng, H. M.; Ren, W.; Bao, Q. *Light: Sci. Appl.* **2016**, *6*, e16204.

(35) Li, X.; Magnuson, C. W.; Venugopal, A.; Tromp, R. M.; Hannon, J. B.; Vogel, E. M.; Colombo, L.; Ruoff, R. S. *J. Am. Chem. Soc.* **2011**, *133* (9), 2816−2819.

(36) Calado, V. E.; Zhu, S.; Goswami, S.; Xu, Q.; Watanabe, K.; Taniguchi, T.; Janssen, G. C. A. M.; Vandersypen, L. M. K. *Appl. Phys. Lett.* **2014**, *104*, 023103.

(37) Velizhanin, K. A. *Phys. Rev. B: Condens. Matter Mater. Phys.* **2015**, *91*, 125429.

(38) Nikitin, A. Y.; Low, T.; Martin-Moreno, L. *Phys. Rev. B: Condens. Matter Mater. Phys.* **2014**, *90*, 041407.

(39) Nikitin, A. Y.; Guinea, F.; García-Vidal, F. J.; Martín-Moreno, L. *Phys. Rev. B: Condens. Matter Mater. Phys.* **2011**, *84*, 161407.

(40) Christensen, J.; Manjavacas, A.; Thongrattanasiri, S.; Koppens, F. H. L.; García de Abajo, F. J. *ACS Nano* **2012**, *6*, 431−440.

(41) He, S.; Zhang, X.; He, Y. *Opt. Express* **2013**, *21*, 30664−30673.

DOI: 10.1021/acs.nanolett.7b02029
Nano Lett. 2017, 17, 5423−5428

Supporting Information
Imaging the Localized Plasmon Resonance Modes in Graphene Nanoribbons

F. Hu[1#], Y. Luan[1#], Z, Fei[1]*, I. Z. Palubski[1], M. D. Goldflam[2,3], S. Dai[2], J.-S. Wu[2], K. W. Post[2], G.C.A.M. Janssen[4], M. M. Fogler[2], D. N. Basov[2,5]

[1]Department of Physics and Astronomy, U.S. DOE Ames Laboratory, Iowa State University, Ames, Iowa, 50011, USA
[2]Department of Physics, University of California at San Diego, La Jolla, California 92093, USA
[3]Sandia National Laboratories, Albuquerque, New Mexico 87185, USA
[4]Department of Precision and Microsystems Engineering, Delft University of Technology, Mekelweg 2, 2628 CD Delft, Netherland
[5]Department of Physics, Columbia University, New York, New York, 10027, USA

[#]These authors contributed equally to this work.

*Email: (Z.F.) zfei@iastate.edu.

1. Experimental details

In order to perform nano-infrared (IR) imaging of graphene nanoribbons (GNRs), we employed the scattering-type scanning near-field optical microscopy (s-SNOM). Our s-SNOM apparatus (Neaspec) is based on an atomic force microscope (AFM) operating in the tapping mode. Measurements were acquired at an AFM tapping frequency of about 270 kHz and a tapping amplitude of about 60 nm. As illustrated in Figure 1 in the main text, we utilized a metalized AFM probe, which is illuminated by a *p*-polarized mid-IR beam from a continuous-wave quantum cascade laser (Daylightsolutions). The angle between the incident beam and AFM tip is about 60 degrees (Figure S1). The illuminated AFM tip generates strong near fields with a wide range of in-plane momenta q. These momenta could exceed the far-field wavevector by two orders of magnitude, thus allowing for energy transfer and momentum matching between the incident photons and excited plasmons. The standard observable of an s-SNOM experiment is s: the near-field scattering amplitude demodulated at the n^{th} ($n = 3$ in the current work) harmonics of the AFM tip oscillation.

Our GNR samples were patterned by electron beam lithography on graphene films grown by the chemical vapor deposition (CVD) method. These CVD graphene samples were then transferred to aluminum oxide (Al_2O_3) substrates by using a sacrifice polymer layer. The Al_2O_3 substrates were grown by atomic layer deposition on silicon wafers. As discussed in detail in Ref. 31 in the main text, the optical phonon resonance of Al_2O_3 is below 1000 cm^{-1}, so we are probing purely the plasmonic signal at our excitation laser frequency $\omega = 1184$ cm^{-1}.

2. Modeling of fringe profiles

The modeled fringe profiles of GNRs (Figure 2 and Figure S2) were obtained through a model developed based on Matlab, which evaluates numerically the total radiating dipole (**p**) of the coupled tip-sample system. Note that **p** is induced by both the far-field excitation field and also the field due to the charges on the GNR surface. Dynamic oscillations of these charges correspond to plasmons. In this model, we consider charge distributions in GNRs induced by both the far-field excitations and the polarized tip, which correspond to surface plasmon resonance (SPR) and

surface plasmon polariton (SPP) modes, respectively. As an approximation, we model the s-SNOM tip as a conducting spheroid. The length of the spheroid is 2L and the radius of curvature at the tip ends is a (Figure S1), where a is set to be about 25 nm according to the manufacturer and L = 500 nm. Note that L is not a very sensitive parameter so long as $L >> a$. By calculating **p** at different z_{tip}, we are able to obtain the third harmonic demodulated near-field signal, which is our experimental observable. While calculating **p** at different x_{tip} allows us to plot the line profiles across GNRs. Our modeling considers single GNR with various widths (90, 270 and 380 nm), where graphene is treated as a homogeneous 2D metal with an optical conductivity of σ_{2D}. The optical conductivity was obtained with the random phase approximation method where Fermi energy of graphene was set to be $E_F \approx 0.37$ eV to match our data. Such a high doping is commonly seen for CVD graphene samples at ambient conditions. At our probing frequency (ω = 1184 cm^{-1}), the plasmon wavelength of graphene is estimated to be $\lambda_p \approx 240$ nm on a Al_2O_3 substrate that has a permittivity of $\varepsilon_{Al_2O_3} = 1.6 + 0.17i$ according to Ref. 31 in the main text. In the modeling, we assume no position dependence along the y direction.

3. Comsol simulations

The real-space plasmon field maps of GNRs in Figures 3 and 4 of the main text were obtained by performing the finite-element frequency-domain simulations with the commercial solver Comsol MultiPhysics. For these E_z field simulations, we construct a 3D model, where the s-SNOM tip is again approximated as the conducting spheroid with the same geometric parameters as the Matlab-based model (Figure S1). We considered a GNR with various widths (90, 270 and 380 nm) and a finite length of 2 μm. The finite-length setting here is a reasonable approximation considering the small plasmon propagation length (L_p << 1 μm) of our graphene samples. Graphene is modeled as an effective 3D metal with an effective thickness of d = 5 nm in order to reduce the computation time, and the corresponding 3D optical conductivity is set to be $\sigma_{3D} = \sigma_{2D}/d$. Considering that $d << \lambda_p$, such a treatment is a good approximation when modeling plasmonic responses of graphene. To prove that, we calculate the dispersion diagrams of graphene plasmons with d = 0.335 nm and d = 5 nm (Figure S3). The color in the dispersion diagrams denotes the imaginary part of the reflection coefficient Im(r_p) of the entire sample/substrate system (See Ref. 9 in the main text for details about the dispersion calculations). The bright curves shown in the dispersion plots correspond to graphene plasmons. The interruption of plasmon dispersion below ω = 1000 cm^{-1} is due to the Al_2O_3 phonons (See Ref. 31 in the main text). From the calculated dispersion diagrams, one can see clearly that they are no clear difference in the graphene dispersion calculated with d = 0.335 nm compared to that with d = 5 nm.

The far-field absorption of GNRs (Figure S4) was calculated using a 2D two-port model in Comsol with periodic boundary conditions to simulate GNR arrays. Here the length of GNR is infinite and the distance between adjacent ribbons are equal to ribbon's width. Through this model, we can calculate IR reflectance (R), transmittance (T) and absorption (A = 1 - R - T) of the GNR arrays. The results are shown in Figure S4, where we plot the calculated plasmon absorption versus ribbon width. The three peaks shown in the plot correspond to n = 0, 2, 4 modes as discussed in detail in the main text.

As a finite-element method, Comsol simulations are expected to generate approximate solutions to physical problems. The numerical errors due to the finite-element approximations are directly associated with the finite mesh size (namely the size of individual element). In the case of the 3D model that we used to perform real-space plasmon field simulations, the mesh size on the

graphene surface is roughly 10 nm. With such a mesh setting, we can perform the simulations with a commercial desktop (Dell Optiplex 9020, i7-4790 CPU, 32G RAM) within a reasonable computation time (~ 1 hour per simulation). One could increase computation accuracy by reducing mesh size, but it requires much larger computer memory and longer computation time (reducing the mesh size by half requires ~8 times the memory and computation time).

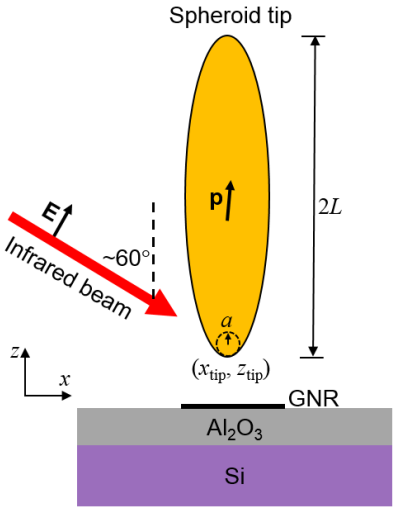

Figure S1. Sketch of the spheroid s-SNOM model for plasmonic simulations of GNRs.

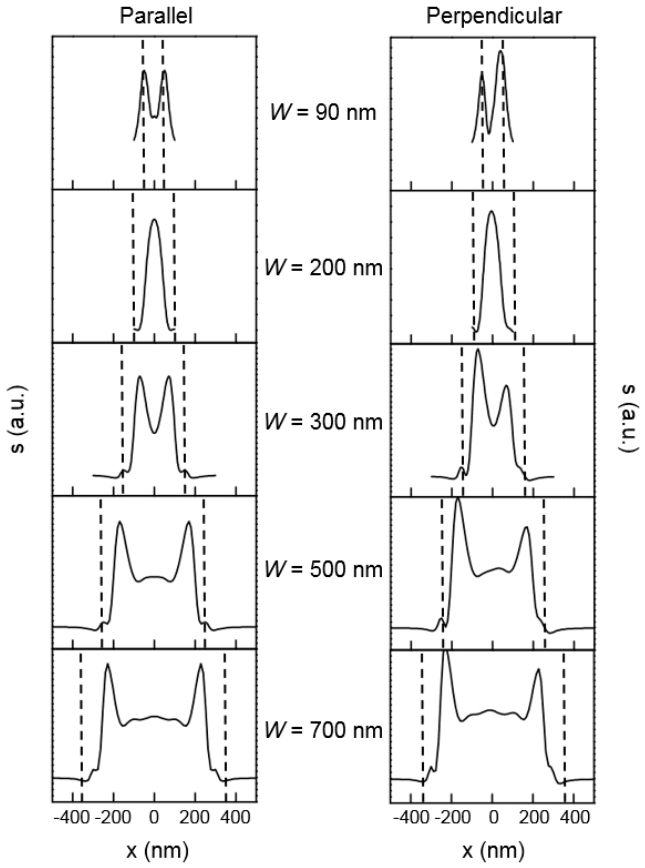

Figure S2. Simulated plasmonic fringe profiles of GNRs with various widths at both parallel (GNR // $\mathbf{E}_{in}$) and perpendicular (GNR $\perp$ $\mathbf{E}_{in}$) configurations. The vertical dashed lines mark the ribbon edge. Note that there are more than two fringes in the case of 500-nm-wide ribbon and 700-nm-wide ribbon. These additional fringes between the two principle fringes are relatively weak due to the plasmon damping.

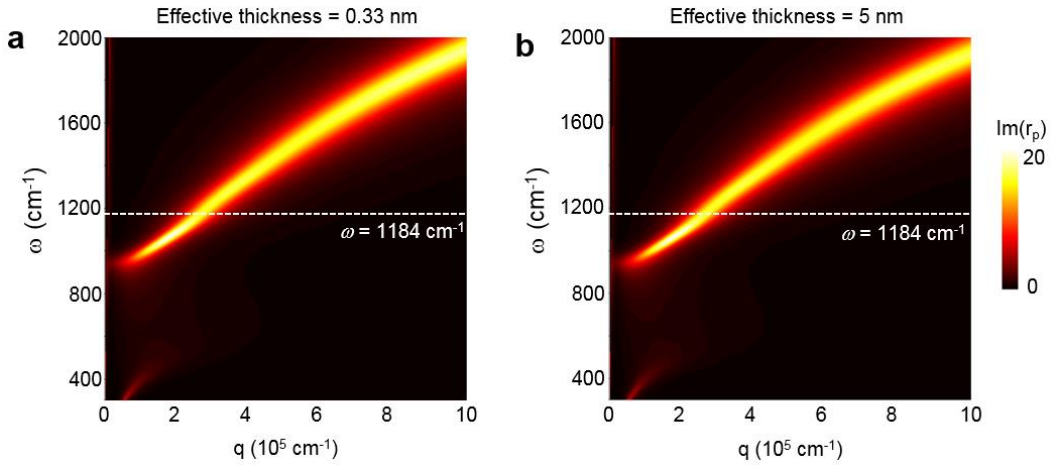

Figure S3. Calculated dispersion diagrams of graphene on Al_2O_3 by assuming an effective thickness of graphene of 0.33 nm (a) and 5 nm (b), respectively. The color denotes the imaginary part of the reflection coefficient Im(r_p) of the entire sample/substrate system (See Ref. 9 in the main text for details about the dispersion calculations).

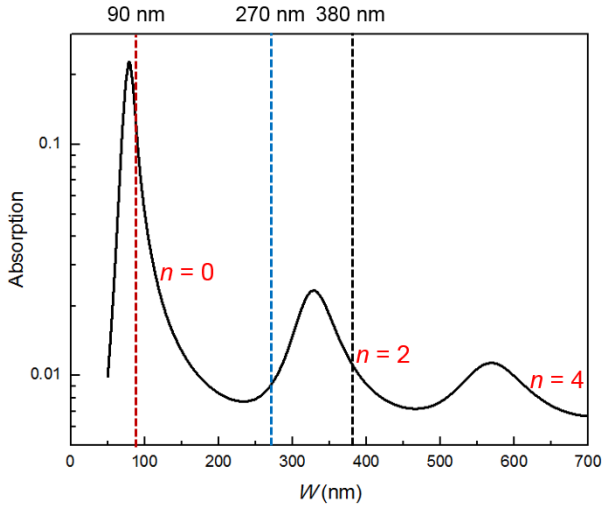

Figure S4. Comsol-simulated far-field IR absorption with respect to the GNR width at our excitation laser frequency ω = 1184 cm^{-1}. The vertical dashed lines mark the widths of GNRs measured in the current work.

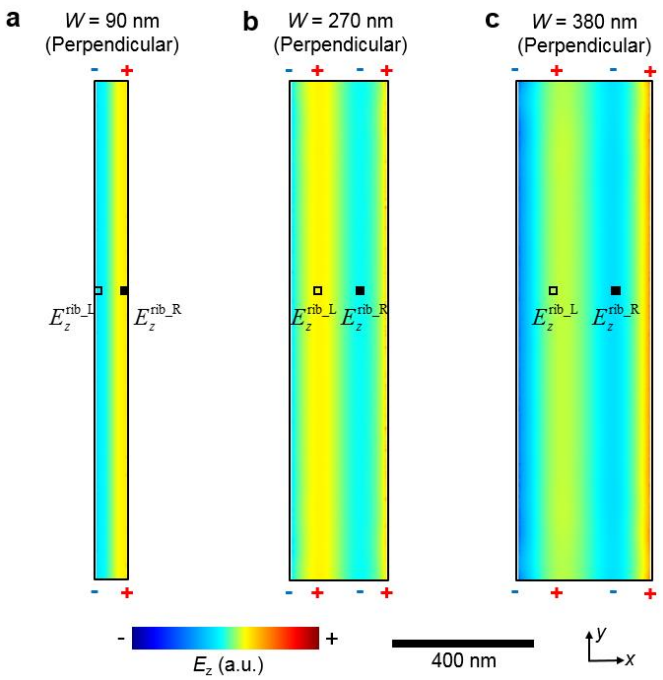

Figure S5. Comsol simulations of the E_z field snapshots of bare GNRs (without tip) with widths of (a) 90 nm, (b) 270 nm and (c) 380 nm under perpendicular excitation configuration. The hollow and solid squares mark the points where we measure the field of the pure SPR mode at the left fringe location ($E_z^{rib\_L}$) and right fringe location ($E_z^{rib\_R}$), respectively.

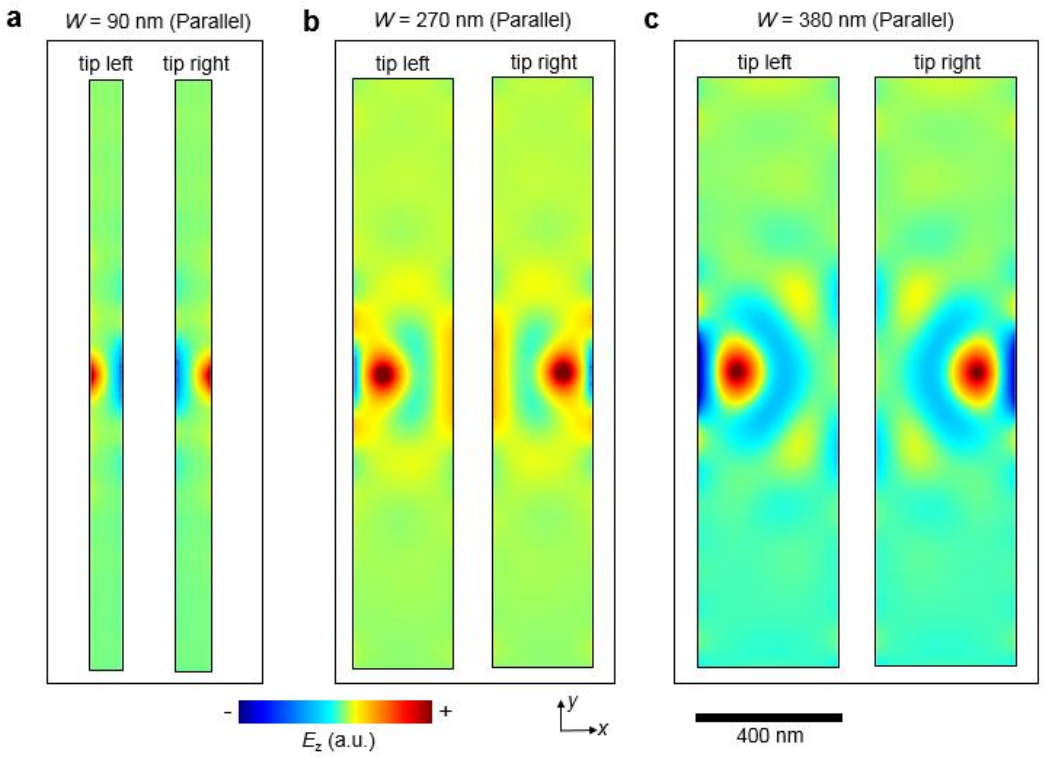

Figure S6. Comsol simulation of the plasmon field maps the GNRs in the parallel configuration. (a-c) Modeled plasmon field maps of GNRs with various widths, where we plot the snapshots of *z*-direction electric field (E_z) right above the graphene surface at $z = 0$. The left and right panels in (a-c) are simulations with tips at the locations of the left and right fringes (see Figures 1 and 2 in the main text), respectively. The tip-sample separation (z_{tip}) is set to be 15 nm. Apparently, the E_z field maps when the tip is at left and at right fringe location are symmetric.

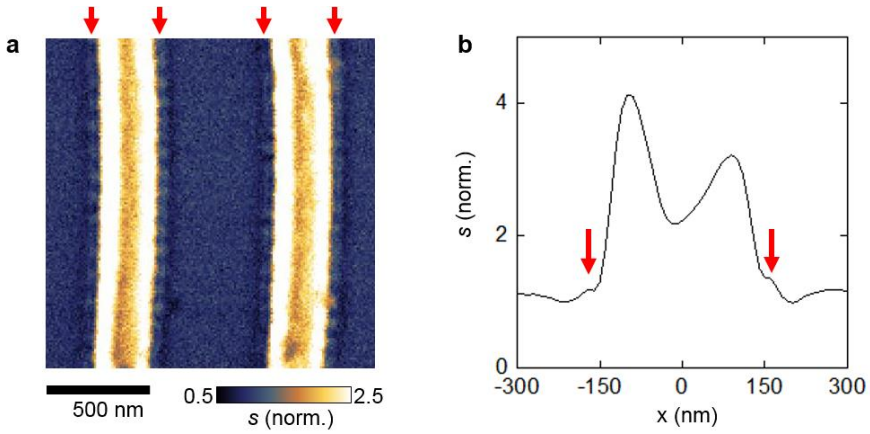

Figure S7. (a) Nano-IR imaging of the 380-nm-wide GNR under perpendicular excitation configuration (replotted from Figure 1f with adjusted color scales). The red arrows mark the lines of edge signal oscillations due to edge plasmons. (b) Line profile taken across the plasmon fringes in (a) (replotted from Figure 2b). The red arrows mark the weak features due to the edge oscillations. Edge oscillations are seen in all near-field images close to lithography-patterned graphene edges, where small edge defects are common. They are generated due to the interference between tip-launched edge plasmons and those reflected or scattered by the edge defects. Due to the low reflection or scattering efficiency of these edge defects, the intensity of these edge oscillation is one order of magnitude weaker compared to the fringes, so edge plasmons only have a minor effect on the fringe profile shown in (b).